Journal of the European Ceramic Society 37 (2017) 1387–1399

Contents lists available at www.sciencedirect.com

Journal of the European Ceramic Society

journal homepage: www.elsevier.com/locate/jeurceramsoc

Average vs. local structure and composition-property phase diagram of $K_{0.5}Na_{0.5}NbO_3$-$Bi_{½}Na_{½}TiO_3$ system

Laijun Liu[a,b,*], Michael Knapp[a], Helmut Ehrenberg[a], Liang Fang[b], Huiqing Fan[c], Ljubomira Ana Schmitt[d], Hartmut Fuess[d], Markus Hoelzel[e], Hichem Dammak[f], Mai Pham Thi[g], Manuel Hinterstein[a,h]

[a] Karlsruhe Institute of Technology (KIT), Institute for Applied Materials (IAM), 76131 Karlsruhe, Germany
[b] College of Materials Science and Engineering, Guilin University of Technology, Guilin 541004, China
[c] School of Materials Science and Engineering, Northwestern Polytechnical University, Xi'an 710072, China
[d] Institute of Materials Science, Technische Universität Darmstadt, D-64287, Germany
[e] Heinz Maier-Leibnitz Zentrum (MLZ), Technische Universität München, Lichtenbergstrasse 1, D-85747 Garching, Germany
[f] Laboratoire Structures, Propriétés et Modélisation des Solides, Ecole Centrale Paris, CNRS- UMR8580, Grande voie des Vignes 92295, Châtenay-Malabry Cedex, France
[g] Thales Research and Technology, Ceramics and Packaging Department, Domaine de Corbeville, 91404 Orsay, France
[h] UNSW Australia, School of Materials Science and Engineering, 2052 Sydney, Australia

ARTICLE INFO

Article history:
Received 28 September 2016
Received in revised form
10 November 2016
Accepted 10 November 2016
Available online 15 November 2016

Keywords:
Structure
Dielectric relaxation
Phase diagram
Lead-free ceramics

ABSTRACT

Phase diagram of the solid solution system $K_{0.5}Na_{0.5}NbO_3$- $Bi_{½}Na_{½}TiO_3$ [(1-x)KNN-xBNT] has been established from dielectric permittivity measurement and structure analyses. The unit cell volumes continuously decrease depending on the composition, while the local structure maintains distortions away from the cubic average structure in the range $0.10 \leq x \leq 0.90$. No clear correspondence for the temperatures of phase transition exists between structural studies and physical properties. The dielectric behavior is depicted successively from normal ferroelectric, diffuse phase transition, re-entrant-like relaxor, relaxor + dipolar glass-like relaxor, BNT-like relaxor with the increase of BNT. A comprehensive composition-property phase diagram for this system has been given to understand the various ferroelectric phenomena. The result could be mainly elucidated by the nanoclusters and the disorder driven nucleation of polar nanoregions contributed by a valence mismatch at one of the cation sites.

1. Introduction

Both sodium potassium niobate ($K_{0.5}Na_{0.5}NbO_3$, abbr. KNN) and sodium bismuth titanate ($Bi_{½}Na_{½}TiO_3$, abbr. BNT) have been considered as a potential replacement for $PbZr_xTi_{1-x}O_3$(PZT) because of their relatively high piezoelectric properties. KNN shows cubic (C) symmetry in space group $Pm\bar{3}m$ above 690 K ($T_{C\text{-}T}$) and tetragonal (T) symmetry ($P4mm$) in the temperature range 470–690 K. The transition from a tetragonal phase to an orthorhombic(O) phase ($Amm2$) occurs at 473 K ($T_{T\text{-}O}$), which in turn transforms to a rhombohedral (R) phase ($R3m$) at ~110 K ($T_{O\text{-}R}$) [1]. Most work on KNN is focused on lowering the high-temperature ferroelastic phase transition (T → O) towards room temperature by the addition of various extra dopants, which is now frequently termed the polymorphic phase transition (PPT) [2–5]. Wang et al.[6] suggested that the main reason for the rapid decrease of $T_{C\text{-}T}$ and the deviation for $T_{C\text{-}T}$ from the Vegard's law is attributed by valence mismatch. Meanwhile, $T_{T\text{-}O}$ and $T_{O\text{-}R}$ are mainly affected by the B-site cations, whereas $T_{C\text{-}T}$ is mainly affected by the A-site cations [6].

The solubility of dopant ions in the KNN lattice is connected with (i) the crystallographic site in which the dopant ion is incorporated and (ii) the charge compensation mechanism for aliovalent dopant ions. In order to maintain electrical neutrality, aliovalent doping often is accompanied by the creation of electronic or ionic defects. Basically ionic conduction leads to increased loss, and results in electrical degradation of the ceramic capacitor. Therefore, acceptor/donor co-doping have proven to be effective mechanisms to overcome this problem.

The structure change of $Bi_{½}Na_{½}TiO_3$ (BNT) with temperature is more complex. At room temperature (RT), it shows a ferroelectric (FE) rhombohedral (R) with a polar $R3c$ space group. Recent studies

* Corresponding author at: Karlsruhe Institute of Technology (KIT), Institute for Applied Materials (IAM), Karlsruhe, 76131, Germany.
E-mail address: ljliu2@163.com (L. Liu).

http://dx.doi.org/10.1016/j.jeurceramsoc.2016.11.024
0955-2219/

showed that the *R* phase is actually monoclinic with space group *Cc* [7,8]. Afterwards referred to as the RT or low temperature phase. X-ray or neutron diffraction indicate that two phase transitions occur above room temperature [9–12]. Firstly, the *R* phase changes to a tetragonal (*T*) one over a broad temperature range (500–700 K), during which the two phases coexist. Vakhrushev et al. considered that the coexistence of the two phases consists of rhombohedral clusters dispersed within tetragonal matrix that grows as temperature decreases, until the rhombohedral phase becomes stable [13]. The tetragonal ferroelastic domain structure is unchanged on cooling from 800 K to 300 K [14]. The cubic (*C*) phase appears at about 800 K up to the melting point.

Isupov [15] has given the physical properties of BNT in detail and emphasized the good convergence of all the results from literature. The temperature dependence of the dielectric permittivity ε¡ä*(T)* shows two anomalies associated with the two phase transitions in BNT [16]. A frequency dependent small hump near 500 K exhibits the relaxor behavior of BNT, then a very broad dielectric maximum situates near 600 K which does not depend on the frequency [17]. It is suggested that a ferroelectric (FE) −antiferroelectric (AFE) phase transition could occur near 500 K. The main dielectric anomaly and depolarization near 600 K originate in the dynamic nature of ferroelectric clusters in the coexisting rhombohedral/tetragonal phases according to neutron diffuse scattering [18]. Above 700 K, the Curie-Weiss law is fulfilled and BNT is clearly paraelectric (PE). The investigation of phase transitions in BNT by transmission electron microscope (TEM) [19] shows that a long-range ordering occurs within the tetragonal phase. The order is still visible in the cubic phase. Therefore, BNT is one of the rare perovskites in which local structure plays an important role on macroscopic physical properties.

Aliovalent substitution in KNN was paid much attention in recent years. Gao et al. [20] reported perovskite $(K_{0.5}Na_{0.5})_{1-3x}La_xNbO_3$ ceramics with $0 \le x \le 0.0175$ possess a orthorhombic symmetry. The observed T_C linearly decreases from 711 to 651 K at a rate of ~34 K/at% as *x* increases from 0 to 0.0175, while $T_{O\text{-}T}$ changes slightly, only having a value of 5 K/at% in 462–501 K. La^{3+}/Ti^{4+} co-doped KNN ceramics [21] show a depressed dielectric peak corresponding to the phase transition from ferroelectric to paraelectric. The transition exhibits the characteristics of a normal diffuse phase transition with an incipient relaxor behavior. Therefore, understanding the solubility mode in co-doped KNN is an important factor to control their electrical properties.

The literature is scarce on studies devoted to the structure-composition-property relationships of co-doped KNN, especially for high concentration doping. Zuo et al. reported a morphotropic phase boundary (MPB) between ferroelectric orthorhombic and rhombohedral phases in the (1-x)KNN-x$BiFeO_3$ solid solution near $x = 0.01–0.02$ [22]. Guo et al. found the crystal structure changed from orthorhombic to tetragonal at $x \sim 0.04$ in (1-x)KNN-x$SrTiO_3$ ceramics, and the dielectric relaxor behavior was induced by doping of TiO_2 and SrO into KNN [23]. The dielectric response shows a typical relaxor/glass-like behavior in the (1-x)KNN-x$SrZrO_3$ system[24]. According to Zuo et al. the (1-x)KNN-xBNT solid solution shows symmetries of orthorhombic at $x \le 0.02$, of tetragonal at $0.03 \le x \le 0.09$, of pseudocubic at $0.09 < x \le 0.20$ and of rhombohedral phases at $x > 0.20$ at room temperature. The MPB between *O* and *T* ferroelectric phases was identified in the composition range of $0.02 < x < 0.03$ [25]. In BNT-rich composition, Kounga et al. reported another MPB between a rhombohedral FE phase ($x > 0.93$) and a tetragonal AFE phase ($x < 0.93$) was found at $x \sim 0.93$ [26]. However, the phase structure is not clear from $x = 0.20$ to $x = 0.90$. The literature provides no information about how the phase structure evolves from rhombohedral ($x \sim 0.20$) to tetragonal ($x \sim 0.93$) and back to rhombohedral ($x \sim 1.00$) with increasing *x*.

Recently, we have investigated the structural phase diagram of the (1-*x*)KNN-*x*BNT system [27]. Synchrotron X-ray diffraction (SXRD) data show the co-solubility of Bi^{3+}/Ti^{4+} into K^+/Nb^{5+} to be infinite. The phase diagram was established by neutron diffraction (ND) and electron diffraction (ED). The room-temperature structures of the orthorhombic ($x \le 0.02$), monoclinic + tetragonal ($0.02 < x \le 0.14$), tetragonal + pseudocubic ($0.14 < x \le 0.87$), tetragonal +rhombohedral ($0.87 < x \le 0.96$) and rhombohedral ($x > 0.96$) phases have been confirmed and subtle changes in the underlying structures were observed. The origin of this change in crystal symmetry was attributed to tilting of octahedra.

More recently, we found that the correlation between the properties and the structure of this system is not yet understood. Furthermore, in the high-concentration substitution range, the physical properties are determined by local structure. Therefore, in this study, we investigate the dielectric behavior of the solid solution (1-*x*)KNN-*x*BNT in details. The origin of ferroelectricity in the system is believed to arise from the displacement of the Ti^{4+}/Nb^{5+} octahedra (and of the cations away from a centrosymmetric position within the TiO_6/NbO_6 octahedra). Ti^{4+} and Nb^{5+} have ionic radii of 0.605 and 0.64 Å, respectively. A more pronounced off-center shift of the smaller Ti atoms is observed in their oxygen octahedral cage in comparison to the larger Nb atom [28]. Then the substitutions of K^+ with Bi^{3+} (exhibiting a stereochemically active lone electron pair) and Nb^{5+} with Ti^{4+} not only disturbs the long-range Nb^{5+} displacement, but also results in substantial local lattice strain, which promotes the appearance of polar nanoregions (PNRs). A detailed investigation on the average/local structure-property relationship for the co-doped (1-*x*)KNN-*x*BNT system is carried out. Average and local structure of the infinite solid solution have been determined using a combination of techniques, including Raman spectroscopy, SXRD, ND and transmission electron microscopy (TEM). Finally, a comprehensive composition-property correlation of (1-x)KNN-xBNT ceramics has been investigated to exhibit the various ferroelectric phenomena in the whole phase diagram.

2. Experiment

The preparation of (1-x)KNN-xBNT (x = 0.00, 0.005, 0.02, 0.04, 0.06, 0.10, 0.20, 0.30, 0.50, 0.70, 0.90, 0.92, 0.94, 0.96, 0.98, 1.00) has been shown in Ref. [27] in detail. The apparent density of the ceramic samples was determined by applying the Archimedes method. The grain size was determined by averaging over the total number of grains in a scanning electron microscopy (SEM) (JSM EMP-800). Silver paste was painted on polished disk-shaped specimens about 0.7 mm thickness and electrodes were fired at 650 °C for 30 min for dielectric measurement. Electrical property measurements were taken with an applied voltage of 500 mV over the frequency range 40 Hz to 1 MHz from 100 K to 800 K using an impedance analyzer (Agilent 4294A).

A Thermo Scientific DXR Raman microscope (Waltham, MA) controlled by the software (Thermo Scientific Omnic) for dispersive Raman measurements was employed. Raman spectra were measured using a 5.0 mW laser emitting at 532 nm, a high-resolution grating with 1200 lines per mm and a confocal pinhole size of 25 μm. The microscope was set to 50 × magnification. Temperature-dependent (*in situ*) Raman experiment was carried out in the range 300–800 K by means of a Linkam MDS600 (Linkam, Tadworth, UK) heating-cooling stage.

High-resolution X-ray diffraction was carried out at the Beamline P02.1 (PETRA III) at HASYLAB (DESY, Hamburg, Germany) [29]. The beamline operates at a fixed energy ~60 keV. The wavelength is 0.20724(5) Å determined by a LaB_6 NIST standard. Powder neutron diffraction was done on the SPODI powder diffractometer at the research reactor FRM-II (Garching, Germany) at an incident wave-

length of 1.548 Å [30]. Data covering a 160° scattering range, were collected by a bank of 80 position-sensitive ^{3}He detectors. Full-profile Rietveld refinements were performed using the software package FULLPROF [30]. The peak profile shape was described by a pseudo-Voigt function [32].

Transmission electron microscopy (TEM) samples were prepared by a standard procedure. The TEM experiments were done on a FEI CM20 Super twin microscope operating under 200 kV using a double tilt holder. Zone axes were indexed according to a cubic structure.

3. Results

3.1. Temperature dependence of dielectric properties

The temperature dependence of the relative dielectric permittivity (ε') for the (1-x)KNN-xBNT ceramics at 1 MHz is shown in Fig. 1(a). For $x \leq 0.02$, two phase-transition peaks are clearly visible at ~650 K (Curie temperature) and ~400 K, corresponding to the cubic to tetragonal transition and the tetragonal to orthorhombic transition, respectively. Both phase transitions shift to lower temperatures with the increase of BNT in this region. Since the compositions exhibit PPT behavior, a coexistence of tetragonal and orthorhombic phases is present in the range of $0.02 < x < 0.04$ near room temperature. For $0.04 \leq x \leq 0.10$, the dielectric anomaly corresponding to the transition from tetragonal to orthorhombic is not visible. The peak of the transition from cubic to tetragonal becomes broad from a normal ferroelectric phase transition to a diffuse phase transition. The temperature corresponding to the maximum (ε'_m) of the real part of dielectric permittivity, T_m, decreases with the increase of BNT. The transition behavior becomes more diffuse with further increasing the BNT content, displacing this composition-induced diffuse transition. Similarly, for $0.10 < x < 0.50$, the phase transition peak becomes very broad and shifts to room temperature. Their associated peaks become continuously wider and depressed, resulting in substantially lower $d\varepsilon_r/dT$ coefficients. The minimum of T_m is ~350 K for the sample of $x = 0.50$. Moreover, ε_m for $x > 0.50$ shifts towards higher temperatures with increasing x. An initial increase in ε'_m is present near $x = 0.96$, which results from the MPB of ferroelectric and anti-ferroelectric phases [26].

Although high-temperature phase transitions are easy to be detected according to relative dielectric permittivity peaks, it is challenging to find low-temperature phase transitions corresponding to peaks of the relative dielectric permittivity. They could be checked based on temperature dependence of the dielectric loss, as shown in Fig. 1(b). A loss peak can be found in the sample of $x = 0.00$ at ~140 K (marked by arrow), which corresponds to a phase transition from orthorhombic to rhombohedral. However, this phase transition cannot be found in the samples of $x = 0.02$ and $x = 0.10$ in the temperature range from 90 K to room temperature. Furthermore, with the increase of BNT up to $x = 0.50$, a new loss anomaly with a very broad peak is present at ~160 K (marked by arrow). Since dielectric anomalies usually associate with phase transitions, polar nanoregions (PNRs) in relaxors [2], space charges [31] or ion hopping polarization [32], the anomaly needs to be approved by structure analysis. In contrast, the temperature of the loss anomaly slightly shifts to low temperatures for $x = 0.90$ and the peak becomes more diffuse. On the other hand, another dielectric anomaly can be found near 370 K (marked by arrow), which associates with the phase transition from a super-paraelectric tetragonal to an antiferroelectric or incommensurate trigonal phase, compared to pure BNT [8,34,35]. With further increase of BNT, the low-temperature loss anomaly moves out of the temperature window for the sample of $x = 0.94$. The temperature dependence of the dielectric anomalies as a function of x is illustrated in Fig. 1(c). T_C or T_m decreases almost linearly at a rate of −15.7 K/at% (Bi^{3+} and Ti^{4+}) for $x \leq 0.10$. Above $x > 0.90$, the temperature of the dielectric permittivity anomaly increases at +13.2 K/at% (Bi^{3+} and Ti^{4+}). At $x = 0.50$, T_C reaches a minimum of ~350 K.

In addition, Fig. 1(d) provides SEM micrographs of polished cross-sections after thermal etching of (1-x)KNN-xBNT ceramics with $x = 0.00$, 0.005, 0.06, and 1.00. Trace impurities and pores can be observed on the samples $x = 0.00$ and 0.005. The sample $x = 0.06$ appears homogeneous microstructure and almost fully dense without apparent pores. Addition of BNT has significant influence on the grain size while small impact on the density of the ceramics. The average grain size of the samples decreases from 7.6 μm to 0.3 μm with the increase of BNT content to 0.06. In the BNT side ($x \geq 0.90$), however, the average grain size increases to 3.5 μm. The relative density is 95% ± 3% in all compositions.

The relative dielectric permittivity (ε') above T_C or T_m is described by a modified Curie-Weiss law [36]:

$$\frac{1}{\varepsilon'} - \frac{1}{\varepsilon_m} = \frac{(T - T_m)^\gamma}{C}, \quad (1)$$

where C is the Curie constant and γ is called diffuseness degree ranging between 1 and 2. Normally, $\gamma = 1$ describes a Curie-Weiss behavior of normal ferroelectrics, while $\gamma = 2$ is valid for a classical ferroelectric relaxor. Based on plots of $\varepsilon'(T)$ at 1 MHz, the relations between $\ln(1/\varepsilon' - 1/\varepsilon_m)$ and $\ln(T - T_m)$ are plotted in Fig. 2a. A linear relationship is observed for all samples. The slope of the fitting curves is used to determine γ values. The γ values increase from 1.01 for $x = 0$ to 1.94 for $x = 0.50$ and then decrease to 1.77 for $x = 1.0$. Fig. 2b shows the plots of γ against x in log scale. Three different regions with different log-behaviors are clearly discernible. This indicates a continuous transition from normal ferroelectric ($x = 0$) to relaxor ferroelectric ($x = 0.5$) with turning point at $x = 0.06$. Furthermore, the BNT-rich composition exhibits a mixed relaxor-normal ferroelectric behavior.

The general dielectric behavior of (1-x)KNN-xBNT ceramics can be separated into four distinctive categories, as shown in Fig. 3 by four representative compositions. For $x \leq 0.02$, the real part of the relative dielectric permittivity (ε') exhibits two distinct dielectric anomalies, furthermore, frequency dispersion of ε' is not observed (Fig. 3a). For $x = 0.06$, a single dielectric anomaly accompanied by a shoulder below T_m is observed. However, frequency dispersion of ε' at temperatures below ε'_m is found (Fig. 3b). For $x = 0.50$, only a single dielectric anomaly is observed. Similar to canonical relaxors, this dielectric peak does not correspond to any changes of macroscopic structure symmetry, but is attributed to the relaxation of PNRs (Fig. 3c). Additionally, a dielectric relaxation with strong frequency dispersion is attributed to space charge polarization at high temperatures [37]. Finally, the ε' for $x \geq 0.90$ ceramics is similar to pure BNT (Fig. 3d). BNT undergoes three successive phase transitions: cubic structure to tetragonal at 813 K and finally to rhombohedral structure below 573 K during cooling from high temperature. In the temperature range 573–673 K a phase coexistence of rhombohedral and tetragonal occurs [38]. The first dielectric anomaly around 590 K is associated with the onset of an antiferroelectric state. The second anomaly with a weak frequency dependency occurs below 500 K corresponding to the transition from tetragonal to rhombohedral.

Dipolar-glass-like relaxor and re-entrant-like relaxor behavior are found in the samples $0.02 < x < 0.90$. Significant frequency dispersion is clear in the temperature range of 150–350 K for $x = 0.20$ and $x = 0.50$. The temperature dependence of the imaginary part of dielectric permittivity (ε'') at different frequencies is presented in Fig. 3. Figs. 3e and 3 g show that the dispersion in ε'' is greatly reduced at higher temperatures, indicating that the frequency dependence results from dipolar-glass-like relaxor rather than the

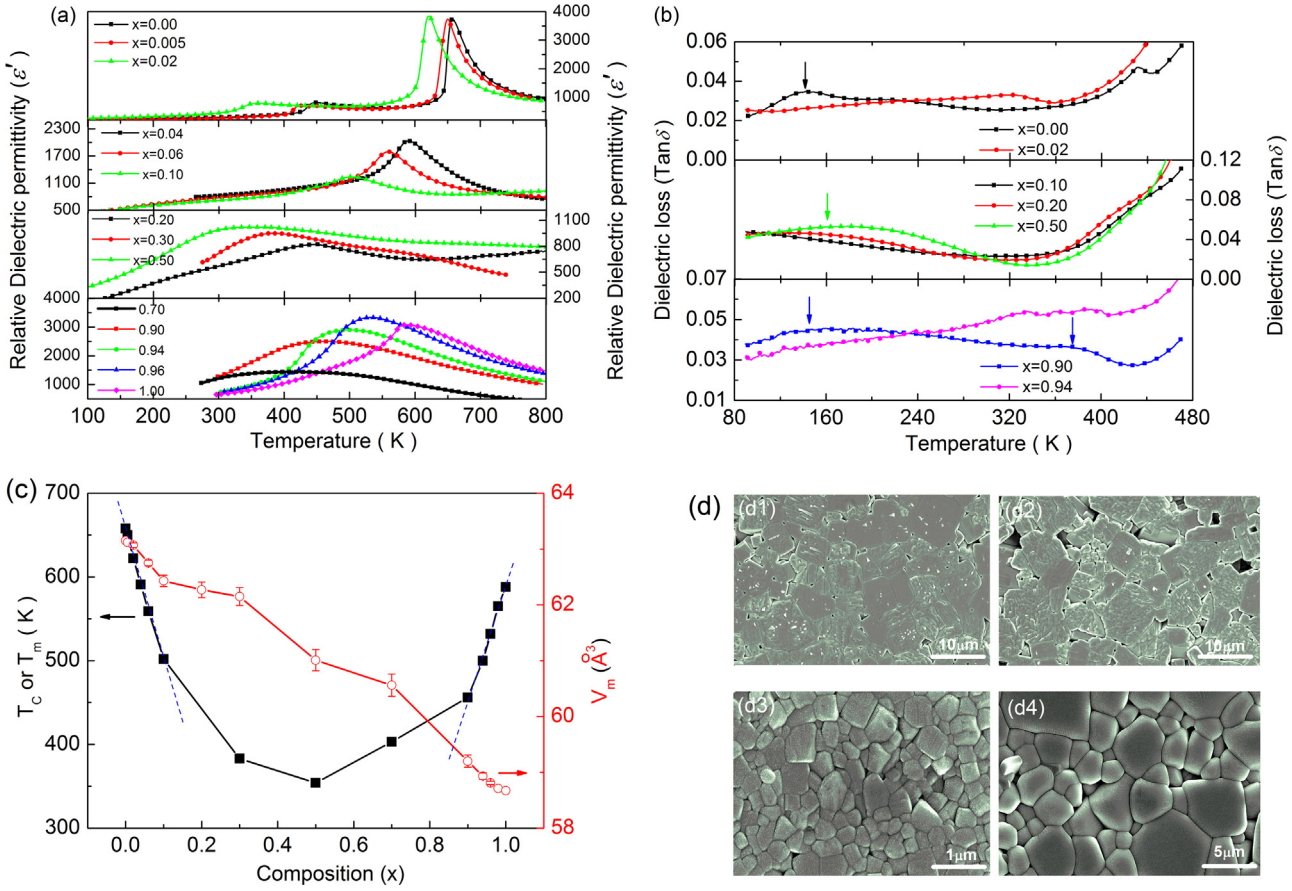

Fig. 1. Temperature variation of the relative dielectric permittivity (ε') (a) and dielectric loss ($\tan\delta$) (b) at 1 MHz of (1-x)KNN-xBNT ceramics. (c) compositional dependence of T_C (or T_m) and unit cell volume for (1-x)KNN-xBNT system. (d) SEM micrographs of polished cross-sections after thermal etching of (1-x)KNN-xBNT ceramics with $x = 0.00$ (d1), 0.005 (d2), 0.06 (d3), and 1.00 (d4).

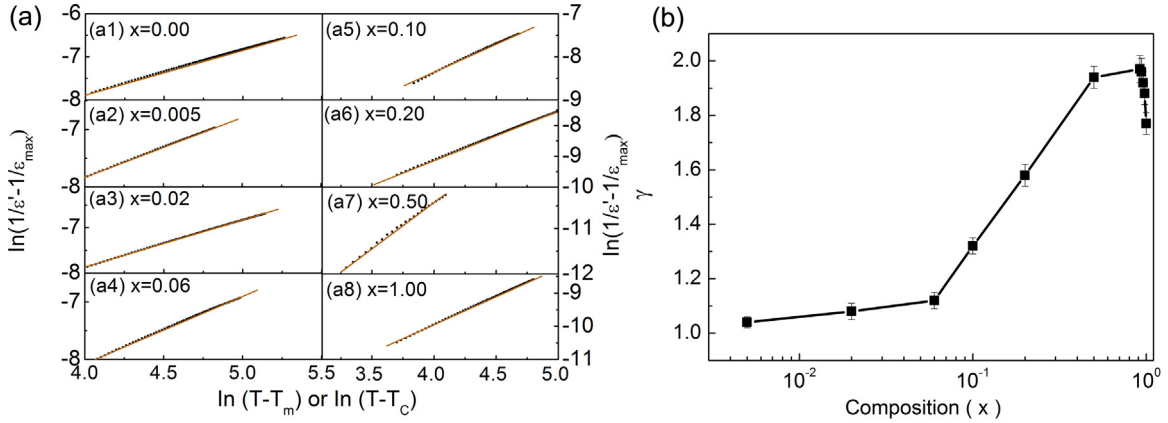

Fig. 2. (a) $\ln(1/\varepsilon' - 1/\varepsilon_m)$ as a function of $\ln(T - T_m)$ at 1 MHz for the (1-x)KNN-xBNT ceramics (symbols: experimental data; solid line: fitting to modified Curie-Weiss law). (b) Plot of γ against x in log scale.

effect of space charges. It is easy to locate the temperature of the permittivity maximum of (T_m'') in the imaginary part of the dielectric permittivity. The dependence of T_m'' on frequencies can be fitted to the Vogel-Fulcher law [39]

$$f = f_0 \exp\left[\frac{-E_a}{k_B(T - T_f)}\right] \quad (2)$$

where T_f is the freezing temperature. k_B the Boltzmann constant. E_a the activation energy attributed to polarization fluctuation of an isolated micropolar region. f_0 is the Debye frequency. T_f can be thought of as the temperature below which thermal energy is no longer sufficient to permit dipolar cluster dynamics in relaxor ferroelectrics.

The fitting results are shown in Fig. 3f and h. The satisfaction of the Vogel-Fulcher law indicates that the ferroelectric relaxor behavior in the compositions is a typical dipolar-glass-like and thermally activated process [40,41]. The fitting results are: $f_0 = 5.99 \times 10^9$ Hz, $E_a = 0.076$ eV, $T_f = 129.8$ K for $x = 0.20$, and $f_0 = 8.92 \times 10^{11}$ Hz, $E_a = 0.18$ eV, $T_f = 117.4$ K for $x = 0.50$. It is noted that the E_a of $x = 0.50$ is much higher than that of $x = 0.20$, fur-

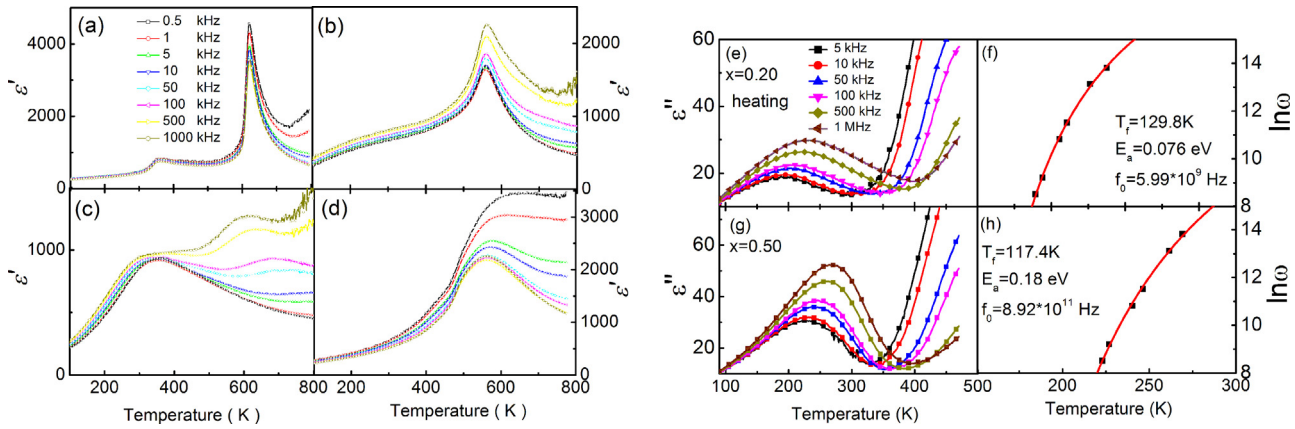

Fig. 3. Temperature dependence of the relative dielectric permittivity (ε') at different frequencies for (1-*x*)KNN-*x*BNT ceramics. (a) $x = 0.02$, (b) $x = 0.06$, (c) $x = 0.50$ and (d) $x = 1.00$. Temperature dependence of the imaginary part of the dielectric permittivity of (e) $x = 0.20$ and (g) $x = 0.50$ at different frequencies. Plots of $\ln\omega$ vs T_m'' of (f) $x = 0.20$ and (h) $x = 0.50$, the solid curves are fitted according to the Vogel-Fulcher relation.

thermore, the T_f of $x = 0.20$ is higher than that of $x = 0.50$ although the T_m'' of the latter is lower. It indicates that the real mechanism of the relaxation between $x = 0.20$ and $x = 0.50$ is different. The temperature dependence of the dielectric permittivity (T_m) of $x = 0.20$ is around 450 K, which is lower than that of $x = 0.06$, meanwhile, similar to $x = 0.06$, the loss peaks with frequency dispersion of $x = 0.20$ also corresponds to the "shoulder" of dielectric permittivity in Fig. 3e. With the increase of BNT, the "shoulder" shifts to high temperature while T_m shifts to low temperature, it vanishes or merges into the relaxation peak in the sample x = 0.50 (see Fig. 3c). The characteristic of the DPT followed by a relaxor "shoulder" in the samples with $0.06 \leq x < 0.50$ indicates the first ferroelectric phase transition of pure KNN subsists in the solid solution. The relaxation observed in 150–300 K occurs below the phase transition temperature T_m, indicating a re-entering behavior. In this case, Ti^{4+} has almost the same ionic size with Nb^{5+}, while the ionic size of Bi^{3+} is much smaller than K^+. Considering that pure BNT has tilted octahedral structure at room temperature, the substitution of BNT for KNN must induce structural distortion. The distortion worsens the phase transition from cubic to tetragonal, as revealed by the lower T_C. Therefore, the relaxor state is contributed by the partial breaking of the ferroelectric long-range ordering (in KNN) by the coupled substitutions of Bi^{3+} and Ti^{4+} ions for K^+ and Nb^{5+} ions with different sizes and charges, respectively. This results in the chemically disordered regions (CDRs) and PNRs responsible for the observed dielectric relaxation.

3.2. Raman spectroscopy

Local symmetry and the dynamics of molecular groups are often detected by Raman spectroscopy. The dynamics of a free NbO_6 group with cubic O_h symmetry are characterized by six normal vibrations ν_i [42]:

$$\Gamma_{vib.} = A_{1g}(Raman) + E_g(Raman) + 2T_{1u}(IR) + T_{2g}(Raman) + T_{2u}(silent) \quad (3)$$

The ν_1 vibration represents Nb—O bonds vibration, which is related to symmetric A_{1g} type mode; ν_2 represents doubly degenerated E_g vibrations of O—Nb—O bonds; ν_3 is a triply degenerated T_{1u} vibration of Nb-O bonds. Stretching modes of the NbO_6 octahedral group belong to the three vibrations. Bending vibration modes refer to: triply degenerated ν_4 of T_{1u} symmetry of the O—Nb—O bonds, triply degenerated ν_5 with T_{2g} symmetry of the O—Nb—O and triply degenerated ν_6 with T_{2u} symmetry of the O—Nb—O bonds. Therefore, characteristic Raman peaks (ν_1, ν_2 and ν_5) in the spectrum of KNN could be related to the internal vibrations of the NbO_6 octahedra. KNN with space group *Amm*2 has 12 optical modes including $4A_1 + 4B_1 + 3B_2 + A_2$ (Raman active normal mode $8A_1 + 4A_2$ if assigned by *Pm* space group).

The Raman spectra of (1-x)KNN-xBNT are presented in Fig. 4(a). On the side of KNN [top of Fig. 4(a), x = 0.00], the spectra are characterized by a symmetric non-degenerated stretching vibration at $\nu_1 \sim 853\ cm^{-1}$. The two lines, which may be assigned to the doubly degenerated ν_2 stretching vibrations at 611 and 547 cm^{-1}, and the band centered at 251 cm^{-1} associates with the triply degenerated ν_5 bending vibration of the NbO_6 group. A sharp band shows up on the low-frequency position of $\sim 193\ cm^{-1}$, but it weakens with the increase of BNT, indicating the tetragonality of the KNN phase decreases [43]. The bands at $<160\ cm^{-1}$ are assigned to the Na^+/K^+ transitional mode and the rotation of the NbO_6 octahedra [44]. On the side of BNT [bottom of Fig. 4(a), x = 1.00], a representative Raman spectrum of unmodified BNT is displayed. The spectrum is agreement with previous reports [45–48], where it was assigned as belonging to the pseudo-rhombohedral *R*3*c* phase, for which a total of 13 Raman-active modes ($\Gamma_{Raman,\ R3c} = 4A_1 + 9E$) are expected.

Four main regions can be discerned in the Raman spectra. The first one at 135 cm^{-1} is a Na/K—O band. Its presence implies that domains with nanometer size exist, because otherwise the phonon lifetime would have been too short to create a defined Raman peak. Such nanodomains should be considered as local $Bi^{3+}TiO_3$ and $(Na_{1-x}K_x)^+TiO_3/(Na_{1-x}K_x)^+NbO_3$ clusters or even one-dimensional chains (but no superstructure) [49]. The second one at $\sim 270\ cm^{-1}$ is dominated by an A_1 mode assigned to Nb/Ti—O vibrations. The mid-wavenumber region in 450–700 cm^{-1} hosts modes related to the vibration of the NbO_6 or TiO_6 octahedra. The high-wavenumber region above 700 cm^{-1} is linked to A_1(LO) and *E*(LO) overlapping bands.

The composition variation of the mode frequencies obtained after deconvoluting the spectra with multiple Lorentz function is plotted in Fig. 4(b). Two clear jumps of the Raman shifts are present in the range of $0.03 < x < 0.06$ and $0.94 < x < 0.96$, corresponding to phase transitions of orthorhombic-tetragonal and AFE-FE, respectively, which agrees with the dielectric analysis (Fig. 1). In addition, three peaks for the Raman shift vs. composition can be found in the bands at $\sim 44\ cm^{-1}$ and $\sim 250\ cm^{-1}$ for $x \sim 0.06$, bands at $\sim 60\ cm^{-1}$ and $\sim 540\ cm^{-1}$ for $x \sim 0.50$ and bands at $\sim 250\ cm^{-1}$ and $\sim 280\ cm^{-1}$ for $x \sim 0.90$. The maximum of mode softening/hardening occurs at x = 0.06, 0.50 and 0.90, displaying phase boundaries or changes of local structure at these compositions.

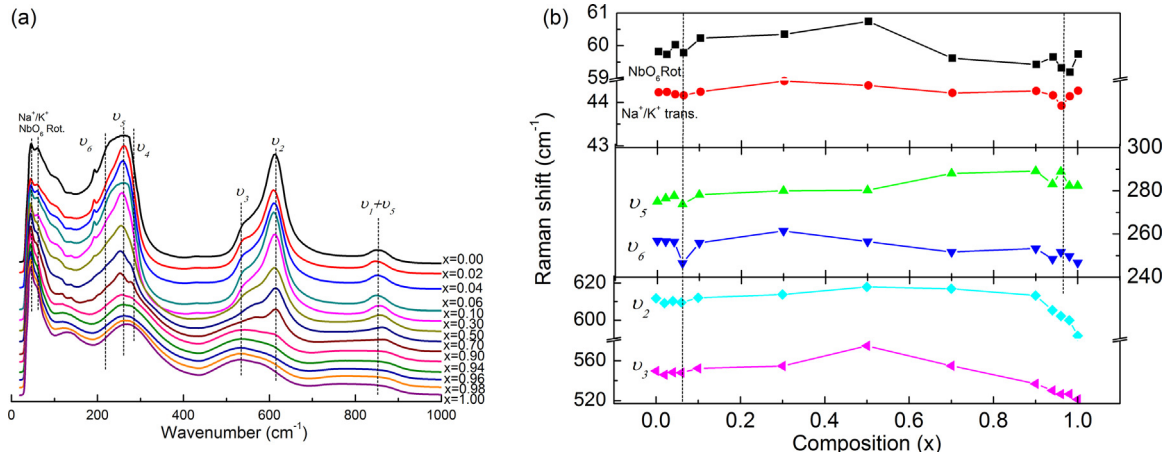

Fig. 4. (a) Raman spectra for (1-*x*)KNN-*x*BNT at room temperature, the shifts and splitting of the phonon bands are due to structural phase transitions between the end-members KNN and BNT. (b) Frequency shifts as determined by the multiple peak fitting of Lorentzian function to the spectra.

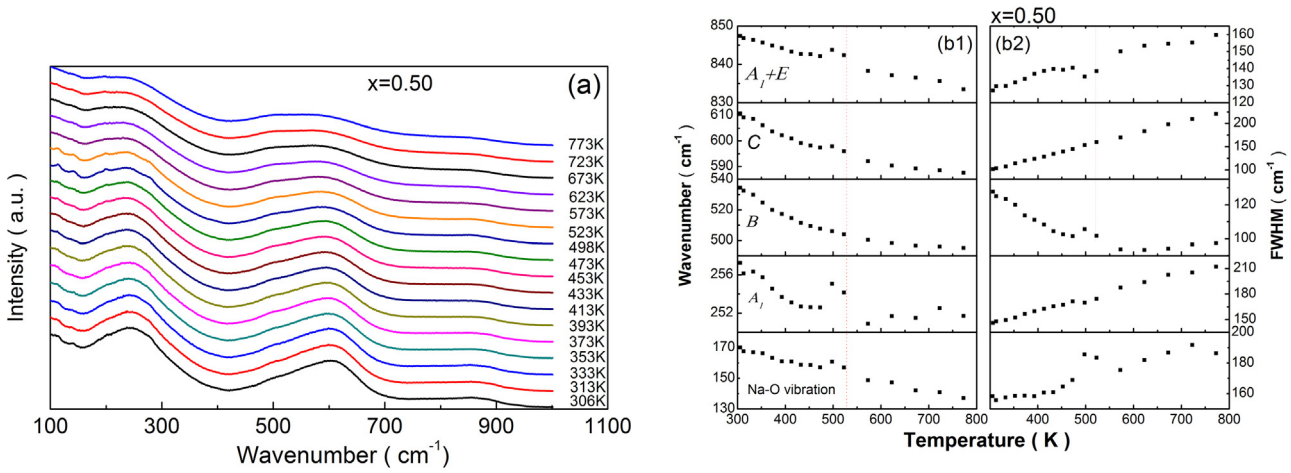

Fig. 5. (a) Raman spectra for the sample of $x = 0.50$ at different temperatures. Band position (b1) and FWHM (b2) change in the Raman spectra as a function of temperature. A significant change of Raman shift indicates an appearance of structure transition.

Since no phase transition can be detected in the temperature dependence of dielectric properties above T_m for $x = 0.50$, here we show the Raman spectra of the sample at different temperatures in Fig. 5(a). The Raman spectra are similar to that of the pure KNN near room temperature, but the lines related to the internal vibrations of the NbO_6 octahedra become more broadened in this composition. All Raman peaks tend to be flat with the increase of temperature but do not vanish even at 773 K. Thus the broadening of the lines results from the increase in the structural disorder in the perovskite lattice. It is found that Raman band positions related to internal vibrations of the NbO_6/TiO_6 octahedra shift into lower values with increasing temperature, as shown in Fig. 5(b1). However, an abnormal Raman shift near 500 K indicates a phase transition could occur because different temperature dependences of the Raman shifts are present on both sides of this temperature. The full width at half maximum (FWHM) of most Raman peaks increases with the increase of temperature except for the band of ~520 cm^{-1} as shown in Fig. 5(b2). The similar anomaly in the Raman shift is also present near 500 K in the temperature dependence of FWHM. Consequently, it provides sufficient evidence that on small length-scales, the symmetry is actually different from cubic symmetry with $Pm\bar{3}m$ space group.

3.3. Powder diffraction

Room temperature synchrotron XRD diffraction data for (1-*x*)KNN-*x*BNT ($x = 0.00, 0.02, 0.06, 0.10, 0.50, 0.94$ and 1.00) powders prepared by solid-state reaction are shown in Fig. 6. A trace of impurities is found in the low solid-solution range, which is agreement with the SEM results as shown in Fig. 1(d). The content of impurities is $1 \sim 2$ *wt%* confirmed by the Rietveld refinement. However, compared with the dielectric behavior as shown in Fig. 1(a) and Fig. 1(b), including dielectric permittivity, Curie temperature, loss factor with Ref [3,25], no obvious difference can be found. Therefore, the trace of impurity phases is not consequential in the observed dielectric behavior/property.

The diffraction patterns for $x = 0.00$ can be indexed based on space group *Amm*2. The sample $x = 0.02$ could be a coexistence of phases of *Amm*2 and *P*4*mm* space group. With further increasing BNT content, a cubic-like structure is present for $0.10 \leq x < 0.90$. The superlattice reflection ½311 becomes more intense with increasing x for $x \geq 0.90$, which indicates the occurrence of an *R*3*c* phase. The compositional dependence of the unit cell volume, V_m, is shown in Fig. 1(c). As a whole, V_m decreases with increasing x since the ionic sizes of Bi^{3+} and Ti^{4+} are smaller than those of K^+ and Nb^{4+}, respectively. The compositional dependence of V_m follows a linear dependence between the end-member compositions ($x \leq 0.10$ and $x \geq 0.90$), in agreement with the empirical Vegard's law. However, a dramatic dependence in the range $0.10 < x < 0.90$ could associate with the complex phase structure. The detailed analysis of the crystal structure is discussed below.

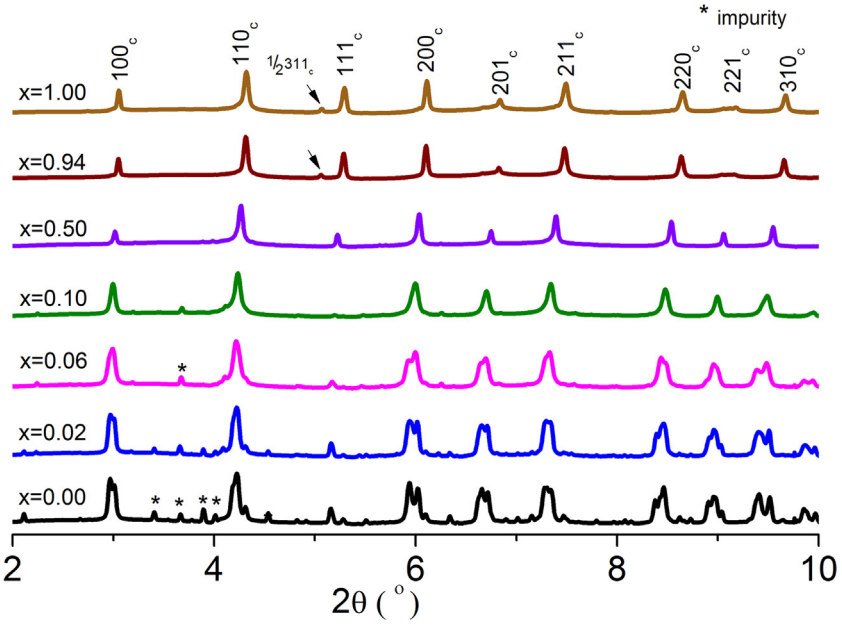

Fig. 6. Powder synchrotron x-ray diffraction patterns of (1-*x*)KNN-*x*BNT ceramics with a logarithmic scale for the intensity. The Miller indices are with respect to a pseudocubic perovskite cell. Impurity is marked by stars and superlattice reflections ½311 are marked by arrows.

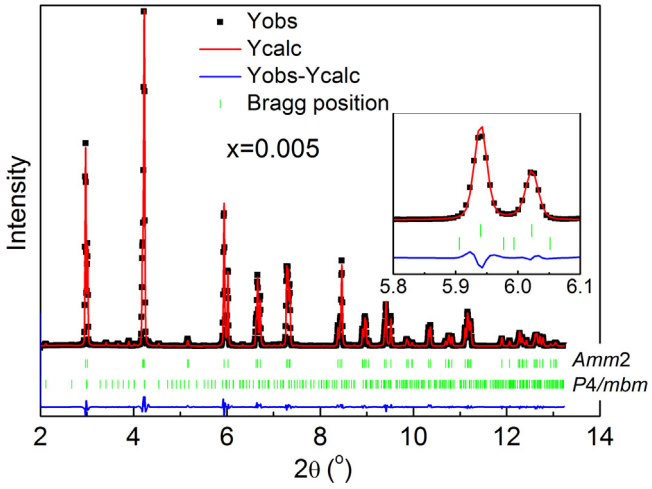

Fig. 7. Rietveld refined synchrotron X-ray diffraction data of the $x = 0.005$, inset shows the 200 reflection [27].

For $x = 0.005$, the room-temperature XRD patterns are analyzed based on an orthorhombic perovskite structure with the space group *Amm*2. The fit between the calculated and observed profiles is satisfactory, as shown in Fig. 7. The fitting results are listed in Table 1. Considering the dielectric and Raman results, the phase structure near this region should be orthorhombic with *Amm*2 space group. With the increase of BNT, the fraction of the tetragonal phase increases, furthermore, the orthorhombic- tetragonal phase transition shifts to room temperature.

Table 1
Structural parameters, fractional atomic coordinates and equivalent isotropic displacement parameters from the synchrotron XRD refinements of the sample $x = 0.005$[27]. The isotropic displacement parameter B_{iso} is in Å^2.

$x = 0.005$	Orthorhombic phase (*Amm*2)			
a–c (Å)	3.9453(4)	5.6412(2)	5.6721(2)	
α, β, γ (o)	90	90	90	
Na/K/Bi x–z B	0	0	0	1.5067(8)
Nb/Ti x–z B	½	0	0.5117(8)	0.2808(1)
O1 x–z B	½	¼	0.2968(8)	1.0675(6)
O2 x–z B	0	0	0.5508(3)	0.6036(7)
R_p, R_{wp}, R_e, χ^2	6.54	8.01	2.67	9.003

Phase fraction of impurity $K_6Nb_{10.88}O_{30}$ is slightly below 2%.

The structure analysis for the sample $x = 0.02$ was carried out by using a structure model of $Pm + P4mm$, as shown in Fig. 8(a). Table 2a gives the refinement results. The R factors are lower than that of $Amm2 + P4mm$ model ($R_p = 7.97\%$, $R_{wp} = 9.90\%$, $R_e = 2.69\%$). The crystal structure consideration was based on the lattice parameters, reflection intensities and lattice distortions, which depend on BNT substitution.

Table 2a
Structural parameters, fractional atomic coordinates and equivalent isotropic displacement parameters from the synchrotron XRD refinements of the sample $x = 0.02$[27]. The isotropic displacement parameter B_{iso} is in Å^2.

$x = 0.02$	Monoclinic phase (*Pm*)				Tetragonal phase (*P4mm*)			
a–c (Å)	4.0055(7)	3.9485(2)	3.9876(7)		3.9665(8)	3.9665(8)	3.9965(7)	
α, β, γ (o)	90	90.261(0)	90		90	90	90	
Na/K/Bi x–z B	0	0	0	1.2115(5)	0	0	0	1.00000
Nb/Ti x–z B	0.4798(8)	½	0.5139(8)	0.3061(9)	½	½	0.4656(1)	0.90000
O1 x–z B	0.5381(3)	½	−0.0114(3)	0.8719(6)	½	½	−0.0549(1)	1.00000
O2 x–z B	−0.0129(1)	½	0.5478(7)	1.1473(9)	½	0	0.4778(6)	1.2543(7)
O3 x–z B	0.5099(9)	0	0.4688(8)	0.7744(9)				
Rp, Rwp, Re, χ2	6.91	8.85	2.69	10.82				
Phase fraction	88%				10%			

Phase fraction of impurity $K_6Nb_{10.88}O_{30}$ is slightly below 2%.

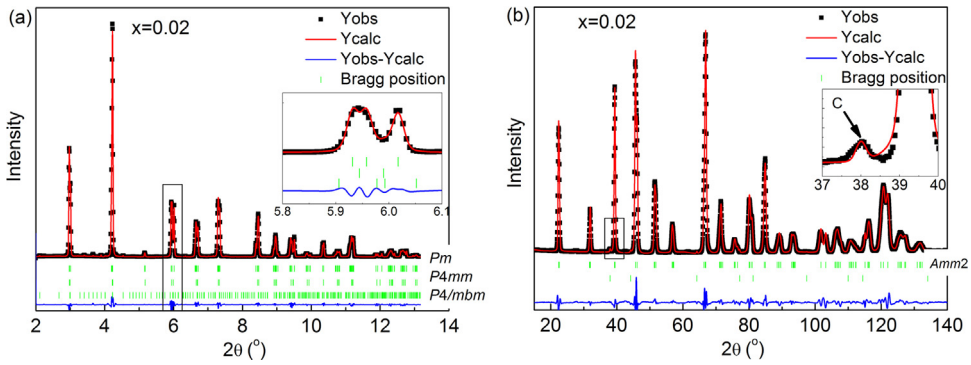

Fig. 8. (a) Rietveld refined synchrotron X-ray diffraction data of $x = 0.02$, inset shows the 200 reflection [27]. (b) Rietveld refined neutron diffraction data of $x = 0.02$ at 4 K. The peak at 2θ=38.1° marked with "C" in the inset is caused by the cryostat setup (inset).

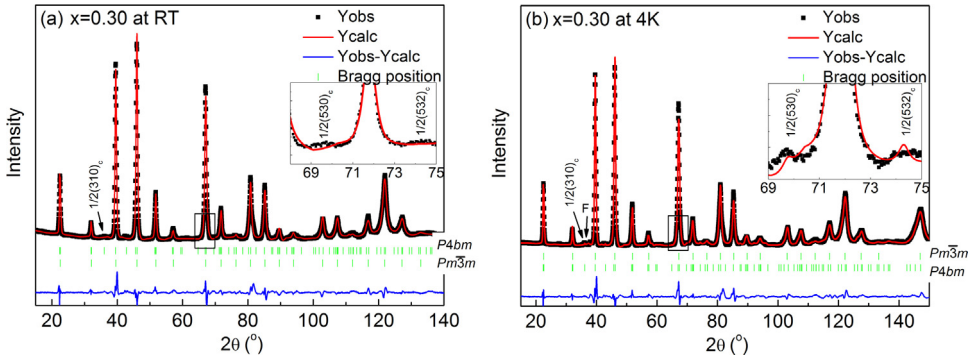

Fig. 9. Rietveld refined neutron diffraction data of $x = 0.30$ at room temperature (a) and at 4 K (b). Inset shows the accountability of the characteristic superlattice reflections ½*ooe* appearing in the *P*4*bm* phase. The peak at 2θ=38.1° marked with "C" in the inset is caused by the cryostat setup.

Table 2b
Structural parameters, fractional atomic coordinates and equivalent isotropic displacement parameters from the neutron refinements of the sample $x = 0.02$ at 4 K[27]. The isotropic displacement parameter B_{iso} is in Å^2.

$x = 0.02$	*4 K Orthorhombic phase (Amm2)*			
a–c (Å)	3.9503(4)	5.6308(7)	5.6583(8)	
α, β, γ (o)	90	90	90	
Na/K/Bi x–z B	0	0	0	1.2236(2)
Nb/Ti x–z B	½	0	0.5067(4)	0.6281(9)
O1 x–z B	½	¼	0.2878(6)	1.0146(3)
O2 x–z B	0	0	0.5419(6)	0.7018(6)
Rp, Rwp, Re, χ2	8.34	9.42	1.90	24.53
Phase fraction	100%			

Dielectric measurements indicate that the orthorhombic-rhombohedral phase transition appears at ~140 K for pure KNN, and it shifts to lower temperatures with the introduction of BNT. Therefore, the low-temperature structure should be identified in the sample $x = 0.02$. Neutron diffraction was carried out at 4 K for the sample $x = 0.02$, as shown in Fig. 8(b). A single phase perovskite structure with *Amm*2 space group was confirmed. The refinement results are given in Table 2b. The reflection marked with an arrow and labeled as *C* ($2\theta = 38.10°$) in pattern associates with the cryostat setup [see inset of Fig. 8(b)]. It suggests the orthorhombic phase of KNN becomes more stable with the introduction of BNT at low temperature.

The structure in the region of $x \geq 0.02$ is much more complex because all SXRD patterns indicate pseudocubic symmetry although dielectric measurements indicate T_m is above room temperature. In order to further confirm the phase structure and fraction, neutron diffraction was carried out for the sample $x = 0.30$ at room temperature and 4 K. Different from the sample of $x = 0.02$, the weak superlattice reflection ½310 is clearly visible near 2θ~36.15° in both, the room-temperature diffraction pattern [Fig. 9(a)] and the low-temperature diffraction pattern [Fig. 9(b)]. The refinement results are shown in Table 3. The presence of ½*ooe* superlattice reflections imply the existence of the tetragonal phase with $a^0a^0c^+$ octahedral tilting [50,51], where "*e*" and "*o*" correspond to even and odd Miller indices, respectively. Considering octahedral tilting of BNT at high temperatures, a *P*4*bm* + *Pm*$\bar{3}$*m* model was used to fit the profile. The fraction of *P*4*bm* in the sample is 74% at room temperature. The fraction of *P*4*bm* slightly increases with the decrease of temperature, which corresponds to the enhancement of ½530 and ½532 superlattice reflections at 4 K. The fit between the observed and calculated profiles by using a *P*4*bm* + *Pm*$\bar{3}$*m* model is of reasonably good quality.

Comparing the neutron diffraction patterns of $x = 0.30$ and $x = 0.90$, the pattern of $x = 0.90$ exhibits ½*ooo* and ½*ooe* superlattice reflections, which belong to *R*3*c* space group and *P*4*bm* space group, respectively [52]. Refinement of neutron data with a mixed *R*3*c* + *P*4*bm* model was performed as shown in Fig. 10. The refinement results are listed in Table 4.

3.4. TEM

Regarding the complex structure of phase-coexistences in the samples, a TEM was performed to reveal the systematic presence or absence of superstructure reflections in two different zone axes. In order to simplify matter, zone axes were indexed corresponding to a cubic structure.

In Fig. 11(a) a bright-field (BF) image of the sample $x = 0.50$ is depicted. The grains show an average size of ~100 nm. The major fraction of those grains show a grainy morphology, which is similar to lead-based relaxor type ferroelectrics [53]. and BNT-BT [54]. Within the grains, areas of several tens of nanometers across are

Table 3
Structural parameters, fractional atomic coordinates and equivalent isotropic displacement parameters from the neutron refinements of the sample $x = 0.30$. The isotropic displacement parameter B_{iso} is in Å^2.

$x = 0.30$ At RT	Tetragonal phase (*P4bm*)				Cubic phase ($Pm\bar{3}m$)			
a–c (Å)	5.5950(5)	5.5950(5)	3.9852(9)		3.9612(8)	3.9612(8)	3.9612(8)	
α, β, γ (o)	90	90	90		90	90	90	
Na/K/Bi x–z B	0	½	0.5534(1)	3.4310(6)	0	0	0	3.6142(3)
Nb/Ti x–z B	0	0	0	0.1789(3)	½	½	½	0.2168(7)
O1 x–z B	0	0	0.5098(7)	0.5132(5)	½	½	0	1.0581(0)
O2 x–z B	0.2570(2)	0.2429(8)	0.0061(6)	0.6145(3)				
Rp, Rwp, Re, χ2	12.50	13.60	4.18	10.54				
Phase fraction	74%				26%			
$x = 0.30$ At 4 K	Tetragonal phase (*P4bm*)				Cubic phase ($Pm\bar{3}m$)			
a–c (Å)	5.5825(9)	5.5950(5)	3.9857(3)		3.9557(1)	3.9557(1)	3.9557(1)	
α, β, γ (o)	90	90)	90		90	90	90	
Na/K/Bi x–z B	0	½	0.5594(4)	3.4310(6)	0	0	0	2.0866(9)
Nb/Ti x–z B	0	0	0	0.1789(3)	½	½	½	0.6178(5)
O1 x–z B	0	0	0.5228(7)	1.5132(5)	½	½	0	2.0487(6)
O2 x–z B	0.2336(2)	0.2663(8)	0.0101(6)	1.6145(3)				
Rp, Rwp, Re, χ2	10.80	11.60	3.01	11.84				
Phase fraction	82%				18%			

Table 4
Structural parameters, fractional atomic coordinates and equivalent isotropic displacement parameters from the neutron refinements of the sample x = 0.90 at 300 K [27]. The isotropic displacement parameter B_{iso} is in Å^2.

$x = 0.90$	Tetragonal phase (*P4bm*)				Rhombohedral phase (*R3c*)			
a–c (Å)	5.51299(1)	5.5117(3)	3.8974(2)		5.5120(4)	5.5120(4)	13.514(9)	
α, β, γ (o)	90	90	90		90	90	120	
Na/K/Bi x–z B	0	½	0.5777(6)	3.7171(5)	0	0	0.2573(4)	4.3298(2)
Nb/Ti x–z B	0	0	0	0.9250(1)	0	0	−0.0133(9)	0.9359(8)
O1 x–z B	0	0	0.5396(6)	1.9364(9)	0.1480(2)	0.3251(9)	1/12	3.7436(2)
O2 x–z B	0.2745(7)	0.2254(3)	0.0670(4)	3.2238(1)				
Rp, Rwp, Re, χ2	19.8	12.7	5.21	5.98				
Phase fraction	22%				78%			

observed, showing a lamellar domain-like contrast (marked by an arrow). The inset of Fig. 11(a) shows the SAED of the $[001]_c$ and $[011]_c$ zone axes of x = 0.50. *½ooo* superlattice reflections were not observed in the examined $[011]_c$ zone, however, the *½ooe* superstructure reflections are visible in the [001]c zone axis, which is a clear indication for the existence of in-phase octahedral tilting without an anti-phase tilting of the oxygen octahedra. Fig. 11(b) displays the centered-dark-field (CDF) image of the nanodomains in the sample $x = 0.90$, which was formed with the $½3\bar{1}0$ superlattice diffraction spot in the [130]c zone axis. The nanodomains (bright speckles) with a thin platelet shape parallel to the (001) plane is revealed by the CDF micrograph, which causes streaking of *½ooe* diffraction spots along the ⟨001⟩ direction [inset of Fig. 11(b)]. The matrix with dark contrast could be a mixture of nanodomains of the other two orientational variants [55]. The CDF image reveals the occurrence of nanoregions of ~30–80 nm. The bright regions in this image are related to the superlattice [56]. SAED shows the *½ooo* and *½ooe* superstructure reflections without spot splitting, due to $a^-a^-a^-$ and $a^0a^0c^+$ octahedral tilting, respectively, which is consistent with our neutron diffraction results.

4. Discussion

Evolution of the dielectric behavior of (1-x)KNN-xBNT ceramics is associated with changes to both the overall crystal symmetry and local structure as discussed hereafter. Composition dependence of the Curie temperature and T_m in the (1-x)KNN-xBNT solid solution is detected by means of temperature dependence of dielectric properties (Fig. 1c). It follows the Vegard's law in both KNN-rich side and BNT-rich side, which also is in agreement with the continuous transitions shown in Fig. 2b. The observed non-linear relationship between the critical temperature and the composition deviates from Vegard's law in the mid concentration doping region. It could be explained according to the coupling strength between individual dipoles of the two basic sublattices, KNN and BNT. The main interaction attributes to the identical dipoles in each sublattice [57]. The average lattice symmetry changes from orthorhombic ($x \sim 0.005$) to tetragonal ($x \sim 0.10$), with coexistence of orthorhombic and tetragonal ($0.04 < x < 0.10$), to pseudocubic ($0.10 < x < 0.90$) and rhombohedral ($x \geq 0.90$), as established by Raman spectroscopy (Fig. 4) and SXRD (Fig. 6–8). However, the local structure maintains distortions away from the cubic average structure for $0.10 < x < 0.90$, revealed by ND (Fig. 9 and 10) and SAED (Fig. 11).

Since both A and B site cations influence the phase transitions of cubic-tetragonal and tetragonal-orthorhombic, it is difficult to confirm which cation plays the main role. The ionic radius of Ti^{4+} (0.605 Å) is smaller than that of Nb^{5+}(0.64 Å), meanwhile, the ionic radius of Bi^{3+} (1.36 Å) is smaller than that of K^+ (1.63 Å). Furthermore, aliovalent substitution at both A and B sites will lead to local composition/charge fluctuation. The temperature dependence of the dielectric properties for $x \leq 0.02$ indicates a classical ferroelectric. It suggests that the Bi^{3+} and Ti^{4+} content is insufficient to interrupt completely the long-range ferroelectric coupling. With increasing x, the temperature dependence of ε' shows a single anomaly accompanied by a relaxor-like shoulder below T_m. The relaxor state occurs after the ferroelectric phase transition upon cooling. The re-entrant phenomenon has been reported in (1-x)$BaTiO_3$-x$BiScO_3$ solid solution [58]. Therefore, the relaxor-like behavior below T_m for $0.05 < x < 0.28$ is not directly related to the structural phase transition. Since the symmetry of BNT is very different from KNN, and the crystal chemistry of the solid solution with the coupled substitutions of Bi^{3+} for K^+ and Ti^{3+} for

Nb^{4+} is more complex. The polar clusters develop from a ferroelectric state and re-enterance the frozen disordered phase, rather than from a paraelectric state as in typical relaxor ferroelectrics, *e.g.*, $Pb(Mg_{1/3}Nb_{2/3})O_3$. The mechanism that is responsible for this observation should be studied by piezoresponse force microscopy (PFM) in future work.

Only a single dielectric anomaly is presented in the sample of $x = 0.50$. The dielectric behavior can be referred to as a diffuse phase transition (DPT) but accompanied by a weak frequency dispersion both at T_m and below T_m. The DPT is often associated with macroscopic heterogeneity, whereas the relaxor behavior results from compositional disorder, *i.e.*, disorder caused by the occupancy of equivalent crystallographic sites by different ions. The emergence of the relaxor behavior in the (1-*x*)KNN-*x*BNT system can be explained in terms of the breakdown of long-range ferroelectric interactions, by randomly distributed clusters, which create random electric fields on atomic length scales. The long-range ferroelectric coupling is interrupted due to the substitution of K^+ and Nb^{5+} by Bi^{3+} and Ti^{4+}, respectively. The size and charge differences of the dopants induce local deformations and stresses that prevent evolution of normal long-range ferroelectric order and favor the formation of short-range polar ordering, even result in the change of symmetry (*i.e.* from *P*4*mm* to *P*4*bm*). For the $x \geq 0.90$, the diffuseness degree of dielectric peak decreases exponentially (Fig. 2b) with the increase of BNT although the profile of the temperature dependence of dielectric permittivity is similar to pure BNT. The temperature of the permittivity anomaly increases at +13.2 K/at.% (Bi^{3+} and Ti^{4+}). It indicates the diffusion of K^+ and Nb^{5+} into the host lattice of BNT (Fig. 1c).

In the (1-*x*)KNN-*x*BNT solid solution, component-induced Raman peak broadening occurs, which indicates that higher structural disorder exists in the Ti-O bond of the TiO_6 octahedra and the Nb-O bond of the NbO_6 octahedra with increasing BNT. Such behavior may be associated with an alternation of zones richer in one constituent than the other. The zones normally are at nanometer size scale, in such a way that diffraction cannot reveal a phase separation [48,56]. It is known that Bi^{3+} ions with lone-pair electrons tend to be off-centered, often inducing in-phase and anti-phase octahedral tilting distortions [38]. The change of structure also is reflected in diffraction results, established by ND (Fig. 10) and SAED (Fig. 11). The local distortions are therefore responsible for the appearance of broad modes in the Raman spectra. Since the ionic radius, valence and mass of K^+ are different from those of Bi^{3+} at the

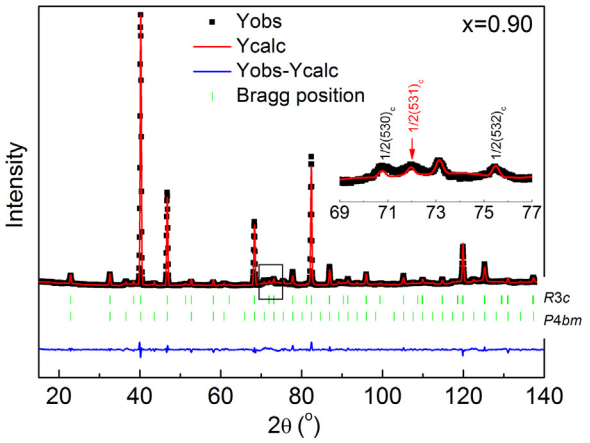

Fig. 10. Rietveld refined neutron diffraction data of $x = 0.90$ at room temperature [27]. Rhombohedral and tetragonal superstructure reflections *½ooe* and *½ooo*, respectively, are visible in the inset.

A site, the introduction of Bi^{3+} into the lattice of KNN will lead to a perturbation of the original energy levels. An increase of energy to optical phonons with lower energy and a decrease of energy to optical phonons of higher energy could be occurred. Finally, the blue-shift and red-shift of the low frequency and high frequency phonons, respectively, will be present on the Raman spectra. However, since the mass of Ti^{4+} is lower than that of Nb^{5+} at the B-site, the shift of high frequency phonons is not obvious. The origin of this discrepancy is not known.

The ν_1–ν_3 vibrations are the stretching modes of the TiO_6 or NbO_6 octahedral group. They become much broader and more symmetrical with increasing temperature in the sample $x = 0.50$ (Fig. 4a). The vibrations were often attributed to second-order effects [59], however, more correctly, they relate to the disorder of Nb/Ti displacement in the octahedra [60]. In the ideal $Pm\bar{3}m$ perovskite structure, all atoms are located in sites having a center of inversion, therefore, no first-order Raman scattering is allowed [61]. On the other hand, the presence of Na^+, K^+ and Bi^{3+} in the A- as well as Nb^{5+} and Ti^{4+} in the B-sites leads to different possible superstructures, for which Raman scattering is allowed (Fig. 5a). The occurrence of these bands provides a strong spectroscopy signal, indicating the occurrence of short range deformation. Furthermore, these bands become more and more broad with the increase of tem-

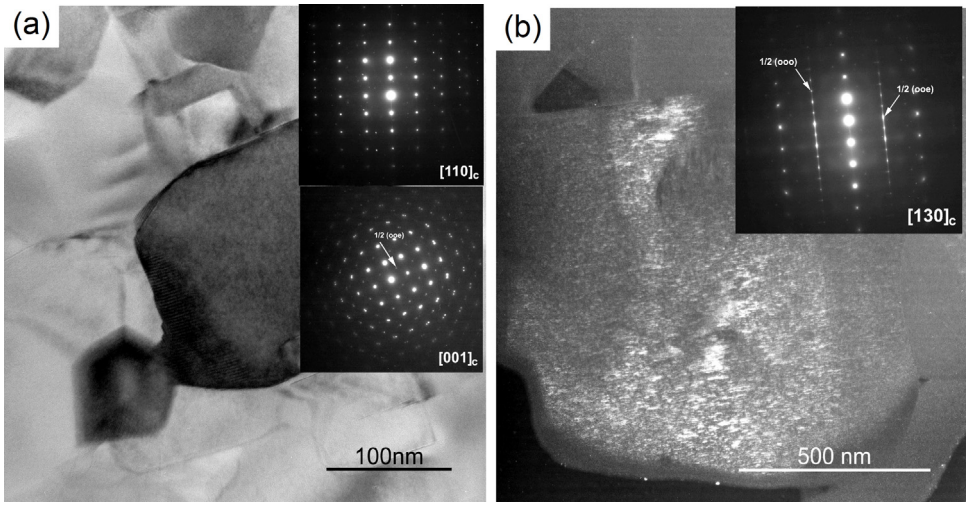

Fig. 11. (a) TEM bright-field image showing the typical subgrain morphology of $x = 0.50$. Inset, SAED patterns of the $[001]_c$ and $[011]_c$ zone axes. The arrow indicates the *½ooe* superstructure reflection. (b) TEM dark-field image of $x = 0.50$ revealing the occurrence of nanosized platelets of several tens of nanometers. Inset, SAED patterns of the $[130]_c$ zone axes. Arrows indicate the presence of *½ooe* and *½ooo* superstructure reflections. The white regions in this image are associated with the *½ ooe* superstructure.

perature [Fig. 5(b2)], which indicates probably that PNRs become smaller.

Ionic size arguments can be used to establish the solubility mode of (1-*x*)KNN-*x*BNT. The substitution of Nb^{5+} (r_{vi} = 0.64 Å) by Ti^{4+} (r_{vi} = 0.605 Å) and K^{+} (r_{xii} = 1.64 Å) by Bi^{3+} (r_{vi} = 1.36 Å) is accompanied by decreases of both, the unit cell volume and the tetragonality. Therefore, the room-temperature crystal structure of (1-*x*)KNN-*x*BNT changes from orthorhombic to tetragonal, then to pseudo-cubic. With further increasing *x*, however, $a^0a^0c^+$ and $a^-a^-a^-$ octahedral tilting distortion is present, induced by the off-centered Bi^{3+} ions with lone-pair electrons [38], although the unit cell volume still decreases (Fig. 1c). The appearance of *½ooe* superlattice reflections in the $[001]_c$ SAED pattern for the *x* = 0.50 ceramic and *½ooe* and *½ooo* reflections positions in the $[130]_c$ SAED pattern for the *x* = 0.90 ceramic, as illustrated in Fig. 11, is indicative of a change in crystal symmetry. The former is not discernible from SXRD data but confirmed by ND. These superlattice reflections arise from tilting of the octahedra along one of the principal axes rather than 1:1-type ordering because the difference both in ionic size and in electronegativity between K^+/Nb^{5+} and Bi^{3+}/Ti^{4+} is very small. The tilting of octahedra varies from in-phase octahedral tilting to anti-phase octahedral tilting with the increase of BNT. For pure BNT, low-temperature and high-temperature polar ferroelectric phases exhibit octahedral tilting, which can be described as $a^-a^-a^-$ for the *R*3*c* phase and $a^0a^0c^+$ for the *P*4*bm* phase [38], respectively. The *P*4*bm* phase was called "ferrielectric" phase due to the antiparallel displacements of the cations giving rise to a small P_s [38]. The temperature dependence of relative dielectric permittivity in Fig. 1 shows that T_m decreases with the decrease of BNT content for $x \geq 0.50$, indicating the high-temperature phase (*P*4*bm*) moves to low temperatures. This is in agreement with ND data and TEM results (Fig. 9–11).

The relaxor behavior may associate with BNT-based clusters inside the KNN lattice, which is explained based on the appearance of superlattice reflections (Fig. 11). In principle, BNT-clusters can be detectable by SAED when they reach a sufficiently large correlation length. BNT is known to exhibit both in–phase and anti-phase rotations of octahedra, in this case, the strong intensity of the *½ooe* superlattice reflections should be an indication of large distortions (in-phase tilting) in a region of large correlation length. The simultaneous appearance of *½ooe* and *½ooo* superlattice reflections indicates the coexistence of in-phase tilting and anti-phase tilting. The highly disrupted phase boundaries, as illustrated in Fig. 11(b), may be a manifestation of this effect.

As mentioned above, (1-*x*)KNN-*x*BNT is an infinite solid solution. The solubility of dopants is determined by an energetic balance, which is eventually correlated to differences in ionic charge (electrostatic energy) and ionic radii (elastic energy) of the various cations. Those are also the criterion that determines the ordering degree at A- or B-site in perovskites. Therefore, it is possible that extended solubility may be driven by the occurrence of short-coherent long range ordering or clustering effects [56]. Although SXRD results suggest that (1-*x*)KNN-*x*BNT ceramics adopt cubic symmetry for $0.10 < x < 0.90$, the broad Raman spectra for these samples provide direct evidence that none of the compositions is strictly speaking cubic with $Pm\bar{3}m$, but exhibiting at least on the local scale distortions away from the cubic symmetry. This is similar to the feature of relaxor ferroelectrics which have local polar clusters. Furthermore, Raman bands are also observed in the sample *x* = 0.50 above its T_m [Fig. 5(b1)]. This feature shows B-site cations to be away from centrosymmetric position and corroborates some degree of order-disorder near and above T_m. Therefore, Raman spectra provide strong evidence for the occurrence of short-range deformations.

The self-compensation mechanism of $½K^+ + Nb^{5+} \rightarrow ½Bi^{3+} + Ti^{4+}$ results in the systematic changes of crystal symmetry of (1-*x*)KNN-*x*BNT ceramics with increasing *x*. On the other hand, the normal ferroelectric microdomains typical of orthorhombic KNN and rhombohedral BNT are completely replaced by nanodomains (Fig. 11), similar to those observed in relaxor ferroelectrics. However, it is clear that long-range ferroelectric ordering is disrupted in heavily doped KNN, which leads to a polar nanodomain state or dipolar-glass-like behavior.

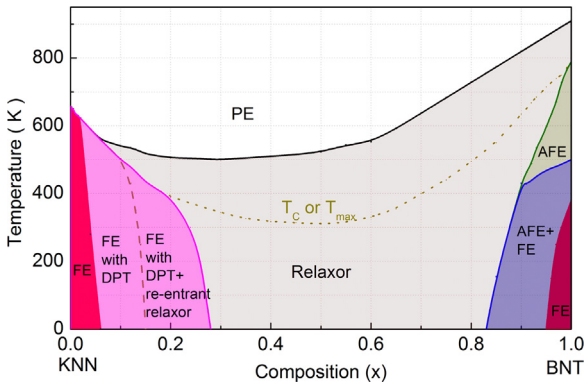

Fig. 12. Phase diagram of (1-*x*)$K_{0.5}Na_{0.5}NbO_3$-*x*$Bi_{½}Na_{½}TiO_3$ system plotted based on results of dielectric, Raman, diffraction measurements.

Fig. 12 shows a phase diagram for (1-*x*)KNN-*x*BNT solid solutions based on our experimental data. The phase diagram in both KNN-rich side and BNT-rich side is in agreement with Ref. [3,6,12,19,25–27,33,34,38,55] The $T_{T\text{-}O}$ and $T_{O\text{-}R}$ of KNN shift significantly to lower temperatures with increasing *x* ($x < 0.05$). The low-temperature state below T_C/T_m is ferroelectric (FE) in compositions with $0.0 \leq x < 0.28$. However, the ferroelectric region includes three parts: FE, FE with DPT and FE with DPT + re-entrant relaxor based phase transition behavior. In the range $0.28 \leq x < 0.82$, canonical relaxor behavior is found while the structure remains macroscopically of cubic symmetry. For $0.82 \leq x < 0.95$, a coexistence of antiferroelectric (AFE) and ferroelectric (FE) phase corresponds to the mixed-phase of *P*4*bm* and *R*3*c*. Finally, compounds with $0.95 \leq x \leq 1.00$ remain in the ferroelectric state.

KNN yields relaxor compositions with a number of interesting features: 1) The relaxor behavior in compositions is not related to nanosized chemically ordered regions; 2) An intermediate state, diffuse phase transitions is undergone from ferroelectric state to relaxor state. 3) Re-entrant behavior occurs in certain compositions. On the BNT-rich side, the relaxors feature: 1) A broad peak of the relative dielectric permittivity, which has nothing to do with a structural transformation; 2) Frequency-dependent anomaly of the relative dielectric permittivity associated with local tetragonal symmetry [62].

The relaxor behavior of KNN is induced by substitutions on both A- and B-sites of the perovskite lattice ABO_3. Firstly, the temperatures of the transition between different ferroelectric phases decrease. Secondly, at a certain concentration of substituting elements all these transitions vanish ($x \sim 0.10$) and the system remains of cubic symmetry ($0.10 \leq x \leq 0.90$). The corresponding peak of $\varepsilon'(T)$ near 0.04 is usually much broader than that in pure KNN, however, without significantly frequency dispersion of T_m. Such behavior is occasionally denoted as a DPT. The modified Curie–Weiss law is better to describe the variety of intermediate states in between purely ferroelectric and relaxor behavior (Fig. 2). At higher substitution, frequency dispersion occurred near T_m matches the Vogel-Fulcher law (Fig. 3f and h). The relaxor state with the distinction between a frequency-independent DPT and a frequency-dependent relaxor-like behavior could associate with different sizes of the PNRs yielding different relaxation times [63].

The re-entrant relaxor behavior is interesting in this system. It suggests a more ordered state develops at higher temperatures firstly before going back to a more disordered state at low temperature [63]. Additionally, the relaxation peak related to the freezing of PNRs happens below another frequency-independent transition attributed to a ferroelectric phase transition [58]. Bharadwaja et al. suggested the re-entrant feature is related to a competitive dipole interaction between local ferroelectric and AFE order and/or local stresses [64]. Consequently, in the (1-*x*)KNN-*x*BNT system, a quenched random electric field (RF) is induced by heterovalent substitution due to the local charge imbalance and the local elastic fields [62]. The field hinders long-range ordering and results in PNRs, finally presenting relaxor behavior.

The charge disorder at A-site randomly occupied by Na^+, Bi^{3+}, and K^+ results in random electric fields, which affect the local balance between the off-center shift of the B-site Nb^{5+}/Ti^{4+} cations and the displacement of the A-site cations. The RF will destroy the long-range order and enhance local dipole correlations, then show different dielectric behavior [65]. This is the basic relationship between dielectric involvement and local structure in the (1-x)KNN-xBNT system.

5. Conclusions

Evolution of the dielectric properties of (1-x)KNN-xBNT ceramics correlates with the crystal structure, local structure, and subgrain microstructure as presented here. The physical phase diagram of the quasi-binary (1-x)KNN-xBNT system was identified. The average lattice symmetry changes as follows:

$$\text{orthorhombic}(x \sim 0.005) \rightarrow \text{tetragonal}(x \sim 0.10)$$

$$\rightarrow \text{pseudocubic}(0.10 < x < 0.90) \rightarrow \text{rhombohedral}(x \geq 0.90)$$

With increasing BNT content the change in dielectric behavior follows the sequence:

$$\text{normalferroelectric} \rightarrow \text{diffusephasetransition}$$

$$\rightarrow \text{re-entrant-likerelaxor} \rightarrow \text{relaxor}$$

$$+\text{dipolar-glass-likerelaxor} \rightarrow \text{BNT-likerelaxor}$$

The plot of diffuseness degree of the dielectric peak against x in log scale exhibits three different regions with different log-behaviors. A continuous transition occurs from normal ferroelectric ($x = 0$) to relaxor ferroelectric ($x = 0.5$) with a turning point at $x = 0.06$. Furthermore, the BNT-rich composition exhibits a mixed relaxor-normal ferroelectric behavior. The local structure maintains distortions away from the cubic average structure for $0.10 < x < 0.90$. A DPT behavior accompanied by a relaxor shoulder below T_m is observed in $0.04 \leq x \leq 0.10$, in agreement with the re-entrant relaxor phenomenon. The single peak of x = 0.50 shows a relaxor-type response. Two additional changes in crystal symmetry (*P4bm* and *R3c*), induced by the off-centering of Bi^{3+}, are observed for $x = 0.50$ and $x = 0.90$, respectively. The simultaneous incorporation of Bi^{3+} and Ti^{4+} in the KNN lattice is accompanied by the disappearance of long-range order ferroelectric domains and the formation of nanoclusters. Raman spectroscopy analysis strongly supports the occurrence of nanoclusters.

Acknowledgments

We acknowledge the support from the fellowship of the Helmholtz Institute and the Karlsruhe Institute of Technology. This work has benefitted from beamtime allocation at P02.1 at PETRA III in Hamburg (Germany) and SPODI at FRM II (Garching) Germany. Financial support from the 'Bundesministerium für Bildung und Forschung (BMBF)' under grant number 05K13VK1, the Australian Research Council (ARC) under grant number DE150100750 and SFB 595, the Natural Science Foundation of China (Nos. 11264010, 51002036, 11564010) and the Natural Science Foundation of Guangxi (Grant No. GA139008) is also acknowledged.

References

[1] J. Tellier, B. Malic, B. Dkhil, D. Jenko, J. Cilensek, M. Kosec, Crystal structure and phase transitions of sodium potassium niobate perovskites, Solid State Sci. 11 (2009) 320–324.
[2] T.R. Shrout, S.J. Zhang, Lead-free piezoelectric ceramics: alternatives for PZT, J. Electroceram. 19 (2007) 111–124.
[3] H. Du, W. Zhou, F. Luo, D. Zhu, S. Qu, Y. Li, Z. Pei, Structure and electrical properties' investigation of $(K_{0.5}Na_{0.5})NbO_3$-$(Bi_{0.5}Na_{0.5})TiO_3$ lead-Free piezoelectric ceramics, J. Phys. D: Appl. Phys. 41 (2008) 115413.
[4] S. Zhang, R. Xia, H. Hao, H. Liu, T.R. Shrout, Mitigation of thermal and fatigue behavior in $K_{0.5}Na_{0.5}NbO_3$-Based lead free piezoceramics, Appl. Phys. Lett. 92 (2008) 152904.
[5] S. Zhang, R. Xia, T.R. Shrout, Modified $(K_{0.5}Na_{0.5})NbO_3$ based lead-free piezoelectrics with broad temperature usage range, Appl. Phys. Lett. 91 (2007) 132913.
[6] R. Wang, H. Bando, M. Itoh, Universality in phase diagram of (K,Na)NbO_3-$MTiO_3$ solid solutions, Appl. Phys. Lett. 95 (2009) 092905.
[7] S. Gorfman, P. Thomas, Evidence for a non-rhombohedral average structure in the lead-free piezoelectric material $Na_{0.5}Bi_{0.5}TiO_3$, J. Appl. Cryst. 43 (2010) 1409–1414.
[8] I. Levin, I.M. Reaney, Nano- and mesoscale structure of $Na_{1/2}Bi_{1/2}TiO_3$: a TEM perspective, Adv. Funct. Mater. 22 (2012) 3445–3452.
[9] J.A. Zvirgzds, P.P. Kapostins, J.V. Zvirgzde, T.V. Kruzina, X-ray study of phase transitions in efrroelectric $Na_{0.5}Bi_{0.5}TiO_3$, Ferroelectrics 40 (1982) 75–77.
[10] J. Suchanicz, J. Kwapulinski, X-ray diffraction study of the phase transitions in $Na_{0.5}Bi_{0.5}TiO_3$, Ferroelectrics 165 (1995) 249–253.
[11] J. Kusz, J. Suchanicz, H.B.J. Warczewski, High temperature X-ray single crystal study of $Na_{1/2}Bi_{1/2}TiO_3$, Phase Trans. 70 (2006) 223–229.
[12] G.O. Jones, P.A. Thomas, The tetragonal phase of $Na_{0.5}Bi_{0.5}TiO_3$–a new variant of the perovskite structure, Acta Cryst. B 56 (2000) 426–430.
[13] S.B. Vakhrushev, V.A. Isupov, B.E. Kvyatkovsky, N.M. Okuneva, I.P. Pronin, G.A. Smolensky, P.P. Syrnikov, Phase transitions and soft modes in sodium bismuth titanate, Ferroelectrics 63 (1985) 153–160.
[14] J. Yao, W. Ge, L. Luo, J. Li, D. Viehland, H. Luo, Hierarchical domains in $Na_{1/2}Bi_{1/2}TiO_3$ single crystals: ferroelectric phase transformations within the geometrical restrictions of a ferroelastic inheritance, Appl. Phys. Lett 96 (2010) 222905.
[15] V.A. Isupov, Ferroelectric $Na_{0.5}Bi_{0.5}TiO_3$ and $K_{0.5}Bi_{0.5}TiO_3$ perovskites and their solid solutions, Ferroelectrics 315 (2005) 123–147.
[16] J. Suchancz, J.-P. Mercurio, P. Marchet, T.V. Kruzina, Axial pressure influence on dielectric and ferroelectric properties of $Na_{0.5}Bi_{0.5}TiO_3$ ceramic, Phys. Status Solidi B 225 (2001) 459–466.
[17] V. Dorcet, P. Marchet, G. Trolliard, Structural and dielectric studies of the $Na_{0.5}Bi_{0.5}TiO_3$ –$BiFeO_3$ system, J. Eur. Ceram. Soc. 27 (2007) 4371–4374.
[18] M. Matsuura, H. Iida, K. Hirota, K. Ohwada, Y. Noguchi, M. Miyayama, Damped soft phonons and diffuse scattering in $(Bi_{1/2}Na_{1/2})TiO_3$, Phys. Rev. B 87 (2013) 064109.
[19] V. Dorcet, G. Trolliard, P. Boullay, Reinvestigation of phase transitions in $Na_{0.5}Bi_{0.5}TiO_3$ by TEM. part I: first order rhombohedral to orthorhombic phase transition, Chem. Mater. 20 (2008) 5061–5073.
[20] D. Gao, K.W. Kwok, D. Lin, H.L.W. Chan, Microstructure and electrical properties of La-modified $K_{0.5}Na_{0.5}NbO_3$ lead-free piezoelectric ceramics, J. Phys. D Appl. Phys. 42 (2009) 035411.
[21] J. Fuentes, J. Portelles, A. Pérez, M.D. Durruthy-Rodríguez, C. Ostos, O. Raymond, J. Heiras, M.P. Cruz, J.M. Siqueiros, Structural and dielectric properties of La- and Ti-modified $K_{0.5}Na_{0.5}NbO_3$ ceramics, Appl. Phys. A 107 (2012) 733–740.
[22] R. Zuo, C. Ye, X. Fang, $Na_{0.5}K_{0.5}NbO_3$-$BiFeO_3$ lead-free piezoelectric ceramics, J. Phys. Chem. Solids 69 (2008) 230–235.
[23] Y. Guo, K. Kakimoto, H. Ohsato, Dielectric and piezoelectric properties of lead-free $(Na_{0.5}K_{0.5})NbO_3$-$SrTiO_3$ ceramics, Solid State Commun. 129 (2004) 279–282.
[24] V. Bobnar, J. Holc, M. Hrovat, M. Kosec, Relaxorlike dielectric dynamics in the lead-free $K_{0.5}Na_{0.5}NbO_3$-$SrZrO_3$ ceramic system, J. Appl. Phys. 101 (2007) 074103.
[25] R. Zuo, X. Fang, C. Ye, Phase structures and electrical properties of new lead-free $(Na_{0.5}K_{0.5})NbO_3$-$(Bi_{0.5}Na_{0.5})TiO_3$ ceramics, Appl. Phys. Lett. 90 (2007) 092904.
[26] A.B. Kounga, S.-T. Zhang, W. Jo, T. Granzow, J. Rödel, Morphotropic phase boundary in (1-x)$Bi_{0.5}Na_{0.5}TiO_3$-x$K_{0.5}Na_{0.5}NbO_3$ lead-free piezoceramics, Appl. Phys. Lett. 92 (2008) 222902.
[27] L. Liu, M. Knapp, H. Ehrenberg, L. Fang, L.A. Schmitt, H. Fuess, M. Hoelzel, M. Hinterstein, The phase diagram of $K_{0.5}Na_{0.5}NbO_3$-$Bi_{½}Na_{½}TiO_3$, J. Appl. Cryst. 49 (2016) 574–584.
[28] I. Grinberg, M.R. Suchomel, P.K. Davies, A.M. Rappe, Predicting morphotropic phase boundary locations and transition temperatures in Pb and Bi-based

perovskite solid solutions from crystal chemical data and first-principles calculations, J. Appl. Phys. 98 (2005) 094111.
[29] M. Herklotz, F. Scheiba, M. Hinterstein, K. Nikolowski, M. Knapp, A.-C. Dippel, L. Giebeler, J. Eckert, H. Ehrenberg, Advances in situ powder diffraction of battery materials: a case study of the new beamline P02.1 at DESY Hamburg, J. Appl. Cryst. 46 (2013) 1117–1127.
[30] M. Hoelzel, A. Senyshyn, N. Juenke, H. Boysen, W. Schmahl, H. Fuess, High-resolution neutron powder diffractometer SPODI at research reactor FRM II, Nucl. Instr. Meth. A 667 (2012) 32–37.
[31] T. Roisnel, J. Rodriguez-Carvajal, WinPLOTR: a windows tool for powder diffraction pattern analysis, Mater. Sci. Forum 118 (2001) 378–381.
[32] P. Thompson, D.E. Cox, J.B. Hastings, Rietveld refinement of DebyeScherrer synchrotron X-ray data from Al_2O_3, J. Appl. Cryst. 20 (1987) 79–83.
[33] L. Liu, Y. Huang, Y. Li, M. Wu, L. Fang, C. Hu, Y. Wang, Oxygen-vacancy- related high-temperature dielectric relaxation and electrical conduction in $0.95\,K_{0.5}Na_{0.5}NbO_3$–$0.05BaZrO_3$ ceramic, Physica B 407 (2012) 136–139.
[34] C.S. Tu, I.G. Siny, V.H. Schmidt, Sequence of dielectric anomalies and high-temperature relaxation behavior in $Na_{1/2}Bi_{1/2}TiO_3$, Phys. Rev. B 49 (1994) 11550.
[35] I.G. Siny, C.S. Tu, V.H. Schmidt, Critical acoustic behavior of the relaxor ferroelectric $Na_{1/2}Bi_{1/2}TiO_3$ in the intertransition region, Phys. Rev. B 51 (1995) 5659.
[36] K. Uchino, S. Nomura, Critical exponents of the dielectric constants in diffused-phase-transition crystals, Ferroelectr. Lett. Sect. 44 (1982) 55–61.
[37] L. Liu, Y. Huang, C. Su, L. Fang, M. Wu, C. Hu, H. Fan, Space-charge relaxation and electrical conduction in $K_{0.5}Na_{0.5}NbO_3$ at high temperatures, Appl. Phys. A 104 (2011) 1047–1051.
[38] G.O. Jones, P.A. Thomas, Investigation of the structure and phase transitions in the novel A-site substituted distorted perovskite compound $Na_{0.5}Bi_{0.5}TiO_3$, Acta Crystallogr. B 58 (2002) 168–178.
[39] D. Viehland, S.J. Jang, L.E. Cross, Freezing of the polarization fluctuation in lead magnesium niobate relaxors, J. Appl. Phys. 68 (1990) 2916.
[40] A.A. Bokov, Z.G. Ye, Freezing of dipole dynamics in relaxor ferroelectric $Pb(Mg_{1/3}Nb_{2/3})O_3$-$PbTiO_3$ as evidenced by dielectric spectroscopy, J. Phys: Condens. Matter 12 (2000) L541–L548.
[41] L. Liu, M. Knapp, L.A. Schmitt, H. Ehrenberg, L. Fang, H. Fuess, M. Hoelzel, M. Hinterstein, Structure and dielectric dispersion in cubic-like $0.5\,K_{0.5}Na_{0.5}NbO_3$ $-0.5Na_{1/2}Bi_{1/2}TiO_3$ ceramic, Europhys. Lett. 114 (2016) 47011.
[42] M. Polomska, B. Hilczer, M. Kosec, B. Malič, Raman scattering studies of lead free (1-x)$K_{0.5}Na_{0.5}NbO_3$-x$SrTiO_3$ relaxors, Ferroelectrics 369 (2008) 149–156.
[43] Z.X. Shen, Z.P. Hu, T.C. Chong, C.Y. Beh, S.H. Tang, M.H. Kuok, Pressure-induced strong mode coupling and phase transitions in $KNbO_3$, Phys. Rev. B 52 (1995) 3976–3980.
[44] Z.X. Shen, X.B. Wang, M.H. Kuok, S.H. Tang, High-pressure Raman study and pressure-induced phase transitions of sodium niobate $NaNbO_3$, J. Raman Spectrosc. 29 (1998) 379–384.
[45] B. Wylie van-Eerd, D. Damjanovic, N. Klein, N. Setter, J. Trodahl, Structural complexity of $Na_{0.5}Bi_{0.5}TiO_3$-$BaTiO_3$ as revealed by Raman spectroscopy, Phys. Rev. B 82 (2010) 104112.
[46] J. Kreisel, A. Glazer, P. Bouvier, G. Lucazeau, High-pressure Raman study of a relaxor ferroelectric: the $Na_{0.5}Bi_{0.5}TiO_3$ perovskite, Phys. Rev. B 63 (2001) 174106.
[47] J. Petzelt, S. Kamba, J. F'abry, D. Noujni, V. Porokhonskyy, A. Pashkin, I. Franke, K. Roleder, J. Suchanicz, R. Klein, G.E. Kugel, Infrared, Raman and high-frequency dielectric spectroscopy and the phase transitions in $Na_{1/2}Bi_{1/2}TiO_3$, J. Phys. Condens. Matter 16 (2004) 2719–2731.
[48] D. Rout, K.-S. Moon, S.-J.L. Kang, I.W. Kim, Dielectric and Raman scattering studies of phase transitions in the (100-x)$Na_{0.5}Bi_{0.5}TiO_3$-x$SrTiO_3$ system, J. Appl. Phys. 108 (2010) 084102.
[49] J. Kreisel, A. Glazer, M.G. Jones, P.A. Thomas, L. Abello, G. Lucazeau, An x-ray diffraction and Raman spectroscopy investigation of A-site substituted perovskite compounds: the $(Na_{1-x}K_x)_{0.5}Bi_{0.5}TiO_3$ ($0 \le x \le 1$) solid solution, J. Phys: Condens. Matter 12 (2000) 3267–3280.
[50] K. Kishida, K. Goto, H. Inui, Electron diffraction of ABX_3 perovskites with both layered ordering of A cations and tilting of BX_6 octahedra, Acta Cryst. B 65 (2009) 405–415.
[51] D.I. Woodward, I.M. Reaney, Electron diffraction of tilted perovskites, Acta Cryst. B 61 (2005) 387–399.
[52] A.M. Glazer, Simple ways of determining perovskite structures, Acta Cryst. A 31 (1975) 756–762.
[53] M. Algueró, J. Ricote, R. Jiménez, P. Ramos, J. Carreaud, B. Dkhil, J.M. Kiat, J. Holc, M. Kosec, Size effect in morphotropic phase boundary $Pb(Mg_{1/3}Nb_{2/3})O_3$- $PbTiO_3$, Appl. Phys. Lett. 91 (2007) 112905.
[54] C. Ma, X. Tan, Phase diagram of unpoled lead-free (1-x)$(Bi_{1/2}Na_{1/2})TiO_3$-x$BaTiO_3$ ceramics, Solid State Commun. 150 (2010) 1497–1500.
[55] V. Dorcet, G. Trolliard, A transmission electron microscopy study of the A-site disordered perovskite $Na_{0.5}Bi_{0.5}TiO_3$, Acta Mater. 56 (2008) 1753–1761.
[56] A. Feteira, D.C. Sinclair, J. Kreisel, Average and local structure of (1-x)$BaTiO_3$-x$LaYO_3$ ($0 \le x \le 0.50$) ceramics, J. Am. Ceram. Soc. 93 (2010) 4174–4181.
[57] C. Aragó, C.L. Wang, J.A. Gonzalo, Deviations from vegard's law in the curie temperature of mixed ferroelectric solid solutions, Ferroelectrics 337 (2006) 233–237.
[58] H. Guo, C. Lei, Z.G. Ye, Re-entrant type relaxor behavior in (1-x)$BaTiO_3$-x$BiScO_3$ solid solution, Appl. Phys. Lett. 92 (2008) 172901.
[59] J. Pokorný, U.M. Pasha, L. Ben, O.P. Thakur, D.C. Sinclair, I.M. Reaney, Use of Raman spectroscopy to determine the site occupancy of dopants in $BaTiO_3$, J. Appl. Phys. 109 (2011) 114110.
[60] Y.J. Jiang, L.Z. Zeng, R.P. Wang, Fundamental and second-order Raman spectra of $BaTiO_3$, J. Raman Spectrosc. 27 (1996) 31.
[61] L. Luisman, A. Feteira, K. Reichmann, Weak-relaxor behaviour in Bi/Yb-doped $KNbO_3$ ceramics, Appl. Phys. Lett. 99 (2011) 192901.
[62] V.V. Shvartsman, D.C. Lupascu, Lead-free relaxor ferroelectrics, J. Am. Ceram. Soc. 95 (2012) 1–26.
[63] X.Y. Wei, Y. Feng, X. Yao, Dielectric relaxation behavior in barium stannate titanate ferroelectric ceramics with diffused phase transition, Appl. Phys. Lett. 83 (2003) 2031.
[64] S.S.N. Bharadwaja, J.R. Kim, H. Ogihara, L.E. Cross, S. Trolier-McKinstry, C.A. Randall, Critical slowing down mechanism and reentrant dipole glass phenomena in (1-x)$BaTiO_3$-x$BiScO_3$ ($0.1 \le x \le 0.4$): The high energy density dielectrics, Phys. Rev. B 83 (2011) 024106.
[65] W. Kleemann, Random-Field induced antiferromagnetic, ferroelectric and structural domain states, Int. J. Mod. Phys. B 7 (1993) 2469–2507.